Optimizing the chiral Purcell factor for unidirectional single-photon emitters in topological photonic crystal waveguides using inverse design

Eric Nussbaum,* Nir Rotenberg,† and Stephen Hughes‡
Centre for Nanophotonics, Department of Physics, Engineering Physics and Astronomy, Queen's University, Kingston, Ontario, Canada K7L 3N6

(Received 2 June 2022; accepted 2 September 2022; published 21 September 2022)

We present an inverse-design approach to significantly improve the figures of merit for chiral photonics with quantum emitters in topological photonic crystal slab waveguides. Beginning with a topological waveguide mode with a group index of approximately 10 and a maximum forward or backward Purcell factor at a chiral point of less than 0.5, we perform optimizations of the directional Purcell factor. We use a fully three-dimensional guided-mode expansion method to efficiently calculate waveguide band-dispersion properties and modes, while automatic differentiation is employed to calculate the gradient of objective functions. We present two example improved designs: (i) a topological mode with an accessible group index of approximately 30 and a maximum unidirectional Purcell factor at a chiral point greater than 4.5, representing a nearly 10-fold improvement to the Purcell factor, and (ii) a slow-light mode well away from the Brillouin-zone edge with a group index greater than 350 and a maximum unidirectional Purcell factor at a chiral point greater than 45.

DOI: 10.1103/PhysRevA.106.033514

I. INTRODUCTION

Chiral quantum elements play an increasingly important role in quantum optical experiments and technologies [1] as they enable nonreciprocal devices [2–6], quantum logic gates [7,8], and networks [9]. One potential route toward scalable, on-chip chiral elements is photonic crystal waveguides (PCWs) integrated with semiconductor quantum dots (QDs) [10–13]. Photonic crystal waveguides are known to collect nearly all photons emitted by a quantum dot [14] while enhancing this emission [15], providing indistinguishable photons over long timescales [16] and enabling efficient few-photon quantum optical nonlinearities [17]. Chiral interactions arise when a QD with circularly polarized transition dipoles is placed in a region where the guided mode field is circularly polarized [18,19] or when both the dipole and field are elliptically polarized [19], with the direction determined by the matching of the signs of the dipole and field polarizations [20]. This has been demonstrated in conventional PCWs [2] and more recently in topological PCWs [21,22].

A significant issue for exploiting PCWs in quantum photonic circuits is that they suffer from disorder-induced backscattering, which is especially severe in the slow-light regime [23–29] where emission enhancement occurs. Photon transport through topological PCWs is known to be robust against certain symmetry-preserving defects such as 60° bends [21,30–32], although we stress that they are not immune to disorder-induced backscattering [33]. However, they do introduce extra flexibility for potentially reducing backscattering [34] as well as enhancing chiral light-matter interactions, which is the main focus of this work. Despite these potential advantages, the question of how much a topological PCW can enhance chiral interactions remains. Traditionally, PCW designs have been improved using *brute-force* searches across a few parameters [35–39]. This has allowed the slow-light properties of PCWs [36,40] and the quality factors of photonic crystal cavities to be significantly improved. More recently, nanophotonic inverse design has enabled further optimization, leading to robust performance compared to devices designed with conventional methods [41–44]. Instead of relying on the designer's intuition or brute-force searches, inverse design optimizes a large number of parameters describing the device, allowing novel and intuitive designs to be obtained [45].

In this work, we show how to optimize a state-of-the-art topological PCW [21] to enhance quantum chiral interactions. We use shape optimization [42] to demonstrate an order-of-magnitude improvement to the directional Purcell factor. To achieve this task, we use the efficient guided-mode expansion (GME) method [46] to calculate the band structure and modes of PCWs and automatic differentiation to calculate the gradient of objective functions. In Sec. II, we briefly outline the GME method and discuss how the directional Purcell factor is calculated and how we apply inverse design. In Sec. III, the results of two optimizations are presented, one operating at a moderate group index $n_g \approx 30$ and the other operating at a larger group index $n_g \approx 350$. In both cases, single-mode operation, well away from the Brillouin-zone edge, is maintained. Finally, we conclude in Sec. IV. We also present two appendices.

II. GENERAL THEORY AND OPTIMIZATION PROTOCOL

In this section, we describe how we use the GME to efficiently and rapidly optimize complex, topological PCWs without the need for computationally intensive methods such as finite-element or finite-difference time-domain (FDTD)

*eric.nussbaum@queensu.ca
†nir.rotenberg@queensu.ca
‡shughes@queensu.ca

techniques which are at least one order of magnitude slower than the GME method for calculating band structures and Bloch modes. For example, full photonic band structure calculations using the GME can be performed in a few minutes on a standard desktop computer, which can take around 1 day using COMSOL MULTIPHYSICS.

After discussing the GME method for obtaining PCW modes and the band structure, we show how the directional Purcell factor is calculated and then discuss how we apply inverse design to rapidly improve chiral figures of merit.

For high-index-contrast-like (planar) PCWs, the GME is highly accurate for computing the dispersion. Moreover, the GME can also be used to obtain the radiative losses for modes above the light line, using perturbation theory [27,46,47]. In the structures we use below, we consider only the practical area of below-the-light-line modes which formally have no intrinsic losses in the absence of disorder. The role of disorder will be investigated in future work. It is also worth mentioning that the GME can also be used to obtain accurate cavity mode losses [46] and can be used as input to a Bloch mode expansion for computing full three-dimensional (3D) Anderson localization modes [48].

A. Guided-mode expansion method

The GME solves Maxwell's equations by expanding the magnetic field in the basis of the modes of the effective homogeneous slab and then solves the resulting eigenvalue problem [46]. The GME is a 3D vectorial method and, as mentioned previoulsy, is significantly faster than alternative methods such as FDTD and COMSOL for calculating the band structure and modes of PCWs [49]. In this work, we use the GME PYTHON library LEGUME by Minkov *et al.* [42,50]. The main details of the GME method are summarized below.

Within a linear dielectric medium, Maxwell's equations for the electric and magnetic fields, $\boldsymbol{E}(\boldsymbol{r},t)$ and $\boldsymbol{H}(\boldsymbol{r},t)$, respectively, can be rewritten in the frequency domain to obtain an eigenvalue equation. In terms of the magnetic field $\boldsymbol{H}(\boldsymbol{r},\omega)$, one has

$$\nabla\times\left(\frac{1}{\epsilon(\boldsymbol{r})}\nabla\times\boldsymbol{H}(\boldsymbol{r},\omega)\right)=\left(\frac{\omega}{c}\right)^2\boldsymbol{H}(\boldsymbol{r},\omega), \tag{1}$$

where $\epsilon(\boldsymbol{r})$ is the dielectric constant, with the condition $\nabla\cdot\boldsymbol{H}(\boldsymbol{r},\omega)=0$. We assume lossless media and neglect frequency dispersion in the dielectric constant, which is a good assumption for the materials of interest for designing and making PCW waveguide modes. Once the magnetic field is calculated, the electric field is easily obtained from

$$\boldsymbol{E}(\boldsymbol{r},\omega)=\frac{i}{\omega\epsilon_0\epsilon(\boldsymbol{r})}\nabla\times\boldsymbol{H}(\boldsymbol{r},\omega). \tag{2}$$

To solve Eq. (1), the GME method expands the magnetic field into an orthonormal set of basis states as

$$\boldsymbol{H}(\boldsymbol{r},\omega)=\sum_\mu c_\mu\boldsymbol{H}_\mu(\boldsymbol{r}), \tag{3}$$

so Eq. (1) can be written as

$$\sum_\nu\mathcal{H}_{\mu\nu}c_\nu=\frac{\omega^2}{c^2}c_\mu, \tag{4}$$

where the elements of the Hermitian matrix $\mathcal{H}_{\mu\nu}$ are defined as

$$\mathcal{H}_{\mu\nu}=\int\frac{1}{\epsilon(\boldsymbol{r})}[\nabla\times\boldsymbol{H}_\mu^*(\boldsymbol{r})]\cdot[\nabla\times\boldsymbol{H}_\nu(\boldsymbol{r})]d\boldsymbol{r}. \tag{5}$$

To define an appropriate basis set $\boldsymbol{H}_\mu(\boldsymbol{r})$, the GME method uses the guided modes of the effective homogeneous-slab waveguide, with the dielectric constant taken as the spatial average of the dielectric constant in the slab layer of the PCW being studied [46]. The guided modes of the homogeneous slab depend on a wave vector, which can take any value in the slab plane, while the modes of the PCW depend on $\boldsymbol{k}$, which we restrict to the first Brillouin zone. Thus, for the magnetic field at each wave vector, only the effective waveguide modes with wave vector $\boldsymbol{k}+\boldsymbol{G}$ are included in the basis. The guided-mode expansion for the Bloch modes is then

$$\boldsymbol{H}_{\boldsymbol{k}}(\boldsymbol{r})=\sum_{\boldsymbol{G},\alpha}C_{\boldsymbol{k}+\boldsymbol{G},\alpha}\boldsymbol{H}^{\text{guided}}_{\boldsymbol{k}+\boldsymbol{G},\alpha}(\boldsymbol{r}), \tag{6}$$

where $\boldsymbol{H}^{\text{guided}}_{\boldsymbol{k}+\boldsymbol{G},\alpha}(\boldsymbol{r})$ is a guided mode (which is known analytically) of the effective waveguide and α is the index of the guided mode. Since the dielectric is periodic, both the magnetic and electric fields can be written according to Bloch's theorem.

The electric- and magnetic-field Bloch mode can be written as

$$\boldsymbol{E}_{\boldsymbol{k}}(\boldsymbol{r})=\boldsymbol{e}_{\boldsymbol{k}}(\boldsymbol{r})e^{i\boldsymbol{k}\cdot\boldsymbol{r}}, \tag{7}$$

$$\boldsymbol{H}_{\boldsymbol{k}}(\boldsymbol{r})=\boldsymbol{u}_{\boldsymbol{k}}(\boldsymbol{r})e^{i\boldsymbol{k}\cdot\boldsymbol{r}}, \tag{8}$$

where $\boldsymbol{e}_{\boldsymbol{k}}(\boldsymbol{r})$ and $\boldsymbol{u}_{\boldsymbol{k}}(\boldsymbol{r})$ are the electric- and magnetic-field Bloch modes for wave vector $\boldsymbol{k}$ and are normalized according to $\int_{\text{cell}}\epsilon(\boldsymbol{r})|\boldsymbol{e}_{\boldsymbol{k}}(\boldsymbol{r})|^2d\boldsymbol{r}=1$ throughout this paper and the integration is carried out over one unit cell. Note that the GME can also be used to compute intrinsic losses for Bloch modes above the light line [46,47].

B. Purcell factor for a single quantum emitter

The coupling between a point-dipole quantum emitter and a waveguide mode can be calculated from a Green's-function analysis [10,20]. The Green's function for the waveguide mode, describing the response at $\boldsymbol{r}$ to an oscillating dipole at $\boldsymbol{r}_0$, is

$$\begin{aligned}\boldsymbol{G}_w(\boldsymbol{r},\boldsymbol{r}_0,\omega)&=\boldsymbol{G}_f(\boldsymbol{r},\boldsymbol{r}_0,\omega)+\boldsymbol{G}_b(\boldsymbol{r},\boldsymbol{r}_0,\omega)\\&=\frac{ia\omega}{2v_g}[\Theta(x-x_0)\boldsymbol{e}_k(\boldsymbol{r})\otimes\boldsymbol{e}_k^*(\boldsymbol{r}_0)e^{ik(x-x_0)}\\&\quad+\Theta(x_0-x)\boldsymbol{e}_k^*(\boldsymbol{r})\otimes\boldsymbol{e}_k(\boldsymbol{r}_0)e^{-ik(x-x_0)}],\end{aligned} \tag{9}$$

where v_g is the group velocity (magnitude) and Θ is the Heaviside step function. The subscripts refer to backward (b) and forward (f) mode contributions.

The rate of photon emission from a QD exciton into the waveguide mode can be split into forward and backward rates. Representing the dipole as a unit vector $\hat{\boldsymbol{\mu}}$ with dipole mo-

ment d_0, the forward and backward emission rates are [20], respectively,

$$\Gamma_w^f(\boldsymbol{r}_0) = \mathrm{Im}\left[\frac{2d_0^2\hat{\boldsymbol{\mu}}^\dagger \cdot \boldsymbol{G}_f(\boldsymbol{r}_0,\boldsymbol{r}_0,\omega)\cdot\hat{\boldsymbol{\mu}}}{\hbar\epsilon_0}\right], \tag{10}$$

$$\Gamma_w^b(\boldsymbol{r}_0) = \mathrm{Im}\left[\frac{2d_0^2\hat{\boldsymbol{\mu}}^\dagger \cdot \boldsymbol{G}_b(\boldsymbol{r}_0,\boldsymbol{r}_0,\omega)\cdot\hat{\boldsymbol{\mu}}}{\hbar\epsilon_0}\right]. \tag{11}$$

These expressions are valid for lossless media [51]; otherwise, a more careful quantum analysis is needed, where the rate of emission is no longer proportional to the projected local density of states, and one must include additional contributions.

The Purcell factor is defined as $P = \Gamma_w/\Gamma_0$, where

$$\Gamma_0 = \frac{\omega^3 d_0^2\sqrt{\epsilon_s}}{3\hbar\pi\epsilon_0 c^3} \tag{12}$$

is the emission rate into the corresponding homogeneous medium with dielectric constant ϵ_s [10]. Separating the Purcell factor into its forward and backward components,

$$P^f(\boldsymbol{r}_0) = \frac{3\pi c^3 a}{v_g\omega^2\sqrt{\epsilon_s}}\hat{\boldsymbol{\mu}}^\dagger\cdot[\boldsymbol{e}_k(\boldsymbol{r}_0)\otimes\boldsymbol{e}_k^*(\boldsymbol{r}_0)]\cdot\hat{\boldsymbol{\mu}},$$

$$P^b(\boldsymbol{r}_0) = \frac{3\pi c^3 a}{v_g\omega^2\sqrt{\epsilon_s}}\hat{\boldsymbol{\mu}}^\dagger\cdot[\boldsymbol{e}_k^*(\boldsymbol{r}_0)\otimes\boldsymbol{e}_k(\boldsymbol{r}_0)]\cdot\hat{\boldsymbol{\mu}}, \tag{13}$$

where v_g and $\boldsymbol{e}_k$ implicitly depend on frequency.

At a spatial point where the field of the forward-propagating mode is right-circularly polarized (RCP), with unit vector $\hat{\boldsymbol{n}}_R = 2^{-1/2}(\hat{\boldsymbol{x}} + i\hat{\boldsymbol{y}})$, a RCP dipole $\boldsymbol{\mu} = \boldsymbol{\sigma}_+$ will couple to only this mode and not to the one propagating backward; similarly, a left-circularly polarized dipole $\boldsymbol{\mu} = \boldsymbol{\sigma}_-$ placed at the same position will couple to only the backward-propagating mode [20].

With a focus on optimizing chiral photon elements, we also define the *chiral directionality*,

$$C = \frac{P^f - P^b}{P^f + P^b}, \tag{14}$$

as well as the *chiral forward Purcell factor*,

$$\tilde{P}^f = CP^f, \tag{15}$$

which will be used below as representative figures of merit.

C. Inverse-design methodology

Inverse design treats the design process as an optimization problem. Instead of using a heuristic understanding of a specific phenomenon and adjusting a small number of related parameters, inverse design optimizes a large number of device parameters. This can lead to unintuitive designs with significantly better performance than their traditionally designed counterparts [41].

Gradient-based optimization algorithms are usually used in inverse design. To efficiently calculate objective function gradients the adjoint variable method is widely used [42]. However, implementing the adjoint variable method can be extremely difficult with a solver which solves an eigenvalue problem, such as the GME method [42]. Instead, automatic differentiation can be used to calculate the gradient of an arbitrarily complex objective function. An automatic differentiation library tracks all subfunction executions for which the gradient is known and then uses the chain rule to compose the objective-function gradient [42]. In this work, we use the automatic differentiation PYTHON library AUTOGRAD [52]. The GME library that we use, LEGUME, was developed to be compatible with AUTOGRAD, making it straightforward to calculate the gradient of the objective functions based on a GME calculation [42].

Starting from an initial design, shape optimization modifies the boundaries between different materials in order to optimize the objective function. In comparison, topology optimization places fewer constraints on how the material distribution can evolve, including allowing the number of holes to be changed. Shape optimization is therefore well suited to optimizing designs where the general shape is known beforehand [53], while topology optimization can produce remarkably inventive designs.

III. RESULTS

Beginning with a state-of-the-art topological PCW [21], we will exemplify several improved designs. The optimizations are performed in two phases: first, the maximum $\tilde{P}^f$ is optimized for a particular mode and wave vector, and second, the dispersion is optimized for a slow-light region. One design is optimized to operate at an accessible group index $n_g = c/v_g$ of approximately 30, while the other has a region of very slow light with a group index greater than 350 away from the Brillouin-zone edge.

A. Initial design

The optimization is started from a reference topological PCW in which chiral coupling of single QDs to the waveguide mode has been experimentally realized [21] using a promising design. The PCW modes are formed at the interface between two topologically distinct crystals. The two crystals are inversion-symmetry partners and are formed from a hexagonal lattice of unit cells containing two circular holes of different sizes, with radii r_1 and r_2, as shown in Fig. 1(a). Similar designs using triangular holes [54] have also been fabricated [13,32,55,56], and our approach could be applied to these designs as well. However, we have focused on a design with circular holes as they are typically easier to fabricate with small dimensions.

In analogy to topological electronics, the topology of these crystals is related to their Chern number [57], which due to the time-reversal symmetry of this photonic system, is equal to zero. However, this need not be the case for the valley Chern index, which we calculate by partitioning the integration of the Berry curvature,

$$\boldsymbol{\Omega}_n(\boldsymbol{k}) = \nabla_{\boldsymbol{k}} \times i\langle \boldsymbol{u}_{\boldsymbol{k},n} \,|\, \nabla_{\boldsymbol{k}} \,|\, \boldsymbol{u}_{\boldsymbol{k},n}\rangle, \tag{16}$$

where n is the index of the mode over the Brillouin zone, to around only the K or K' valley [31], as shown in Figs. 1(b) and 1(c). For details on how to numerically calculate the Berry curvature, see Ref. [58]. The valley Chern index is $C_V = C_K - C_{K'}$, where, for example, $C_K = \frac{1}{2\pi}\iint_{BZ,K}\Omega_n(\boldsymbol{k})dk^2$ is the integral of the Berry curvature over half the Brillouin zone around

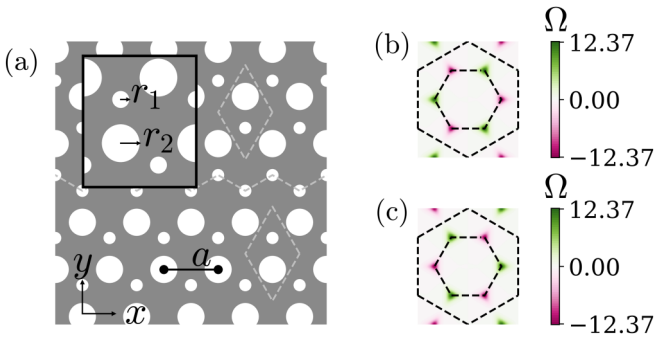

FIG. 1. (a) Schematic of the topological edge-mode waveguide. The direction of propagation x and relevant geometric parameters are indicated. (a) Schematic (top-down view) of the photonic crystal. The rhombic unit cell is outlined. Magnitude of the Berry curvature for the mode below the band gap $\Omega(\boldsymbol{k})$ (in units of $[a^2/4\pi^2]$) for the (b) upper and (c) lower crystals shown in (a) for slab thickness $h = 170$ nm, $a = 250$ nm, $r_1 = 28$ nm, and $r_2 = 62.5$ nm. The outer dashed black line is the edge of the first Brillouin zone, and the inner dashed line's vertices are the K and K' points.

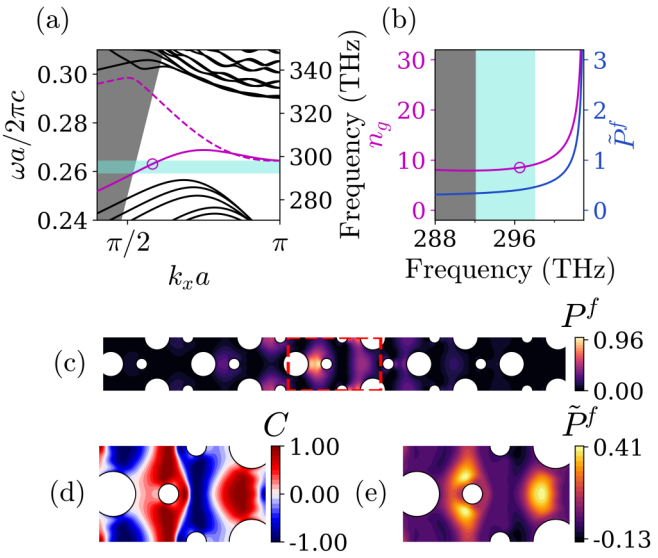

FIG. 2. (a) Band structure for the initial design [21] with $a = 266$ nm. The (NT) guided mode is drawn in solid purple, the second guided mode is drawn in dashed purple, and bulk modes are in black. The NT mode's SM bandwidth is highlighted in turquoise. Additional guided modes existing at the secondary interface at the edge of the GME unit cell have been removed here, as well as in Figs. 3 and 4 (see Appendix A). (b) The group index for the NT mode is drawn in purple, and the maximum chiral forward Purcell factor is drawn with a solid blue line. Frequencies at which the NT mode is above the light line are highlighted in gray. The following fields are calculated at the circles in (a) and (b), where $n_g = 8.5$. The xy-plane cross sections are at the center of the slab. (c) Forward Purcell factor P^f for $\boldsymbol{\mu} = \boldsymbol{\sigma}_-$, (d) the associated chiral directionality C, and (e) the associated chiral forward Purcell factor $\tilde{P}^f$. The red dashed box in (c) encloses the region shown in (d) and (e).

the K valleys. Unlike the Chern number, the valley Chern index is not necessarily quantized [31,58]. The two crystals on each side of the interface have the same $|C_V|$ but with opposite sign. This opposing sign gives rise to valley Hall edge states, which are expected and have been shown to be more robust against defects that do not couple the counterpropagating states [30–32].

This initial topological waveguide is designed to operate near a wavelength of 1000 nm in a 170-nm-thick GaAs (dielectric constant of 11.6) membrane, and so it has a pitch $a = 266$ nm, $r_1 = 28$ nm, and $r_2 = 62.5$ nm [21]. As shown in Fig. 2(a), the initial design has two guided modes in the frequency range of interest. We refer to these modes as trivial (T) and nontrivial (NT) and in what follows focus on the latter. This is because the NT mode has been experimentally demonstrated to support chiral coupling to single QDs and has been used to form triangular ring resonators [21]. Further, as demonstrated in Ref. [21], when a corner is placed in the waveguide, the NT mode propagates around the corner, while the T guided mode is prone to backscattering. We note that, if we begin with the bearded interface in Fig. 1(a) and increase the radius of one of the rows of small holes at the interface to the size of the large holes such that there is a smooth transition to a zigzag interface, then the NT mode remains throughout, while the other guided mode disappears into the bulk bands [21].

For this initial design, we observe that the NT edge state has a single-mode (SM) bandwidth positioned around 296 THz. Within this frequency band, at 296.5 THz, at a spectral separation of 1.6 THz away from the band edge, the mode has a group index $n_g = 8.5$, as shown in Fig. 2(b) by the circle. Although chiral emission into this structure has been observed [21], the calculated P^f map peaks at 0.96 [Fig. 2(c)], demonstrating that this emission is, in fact, suppressed. Worse, the maxima of P^f and C do not overlap for this initial design, and we find a maximal $\tilde{P}^f = 0.41$ [Fig. 2(e)]. In the region where $C \geqslant 0.97$, the maximum forward Purcell factor is $\max(P^f) = 0.41$.

Before optimizing the design, we shift the pitch to $a = 250$ nm to increase the operational frequency to ensure that the optimized design can function around 320 THz, the desired frequency for working with high-quality gallium arsenide quantum dots [12]. However, because of fabrication limits, we do not decrease r_1 below our minimum allowed size of $r_{\min} = 27.5$ nm [21], so we use the same hole sizes in $r_1 = 28$ nm and $r_2 = 62.5$ nm with $a = 250$ nm. We note that changing the hole radii by this amount does not adversely affect the concentration of the Berry curvature with opposite signs at the K and K' points. After the optimization, the periodicity can be increased if it is necessary to decrease the operational frequency, but the periodicity cannot, in general, be further decreased without violating our fabrication-imposed constraints.

B. Optimization

One of our objectives for the optimization is to improve the system's performance as a bright, or rapid, chiral light-matter interface. We therefore demand single-mode operation and consider only positions that are at least 35 nm away from the nearest hole edge to ensure that the QDs can be electrically

gated [59]. Our desired design should have an accessible group index of less than 50 with a Purcell factor, in a region where $C \approx 1$, of approximately 5, which is close to the optimum Purcell factors for enabling efficient pulse-triggered single-photon sources [60–62]. As discussed above and shown in Fig. 2, the maximum chiral Purcell factor for the initial design is 0.41. We are therefore targeting an increase by a factor of approximately 10. With the same restrictions, apart from allowing for a large group index greater than 50, we also seek a design with a maximized chiral forward Purcell factor.

A shape parametrization is used where the position and radii of the 12 holes closest to the interface are allowed to be modified. To ensure the final design can be fabricated, extremely small features must be avoided. Therefore, the minimum allowed hole radius is 27.5 nm, and the minimum allowed distance between hole edges is 40 nm. At the start of each optimization iteration, a projection is applied to the design parameters which transforms designs which violate theses constraints to a similar design which does not. The Adam [63] optimization algorithm is used throughout.

A two-step optimization is performed. The first optimization phase is focused on improving $\max(\tilde{P}^f)$ in a region approximately 35 nm away from the nearest hole edge. The objective function for the first phase is

$$\mathcal{F}_1(\boldsymbol{\gamma}) = \max[G(\boldsymbol{r})\tilde{P}^f(\boldsymbol{r})]G_{\mathrm{SM}}, \tag{17}$$

where $\boldsymbol{\gamma}$ is a vector of the device parameters, $G(\boldsymbol{r})$ is a smooth step function that is equal to 0 inside a hole and approximately 1 more than 35 nm from a hole,

$$G(\boldsymbol{r}) = \frac{1}{1 + e^{-g(r_m(\boldsymbol{r}) - r_s)}}, \tag{18}$$

where $r_m(\boldsymbol{r})$ is the minimum distance to a hole edge, $r_s = 30$ nm and $g = 74\,\mathrm{nm}^{-1}$ are parameters, $G\tilde{P}^f$ is calculated for the NT mode at a fixed wave vector, and G_{SM} encourages a certain magnitude and position of the SM bandwidth. The objective function for the first phase is maximized.

The intermediate design from the first phase is further optimized in a second phase of optimization which is focused on improving the dispersion characteristics for slow-light operation. Two different objective functions are used to obtain two different styles of design. The first is designed to obtain our primary objective of operation at an accessible group index,

$$\mathcal{F}_{2A}(\boldsymbol{\gamma}) = \int_{k_{x,0}}^{k_{x,1}} dk_x (n_g - n_{g,d})^2, \tag{19}$$

where n_g is the group index of the NT mode, $n_{g,d} = 30$ is the desired group index, and the integral is performed over $k_x a = [0.6, 0.9]\pi$. The second is used to obtain a very large n_g inside the NT mode's SM bandwidth,

$$\mathcal{F}_{2B}(\boldsymbol{\gamma}) = \omega_b - \omega_{\mathrm{SM,max}} + \frac{D}{\max_{\mathrm{SM}}(n_g)}, \tag{20}$$

where ω_b is the frequency under the light line, where n_g first changes sign, $\omega_{\mathrm{SM,max}}$ is the maximum frequency of the NT mode's lowest-frequency region of the SM bandwidth, D is a weight, and $\max_{\mathrm{SM}}(n_g)$ is the maximum n_g in the NT mode's lowest region of the SM bandwidth. The objective function B therefore works to make the NT mode's bandwidth entirely SM and to increase the maximum n_g in the SM bandwidth. Both $\mathcal{F}_{2A}(\boldsymbol{\gamma})$ and $\mathcal{F}_{2B}(\boldsymbol{\gamma})$ are minimized.

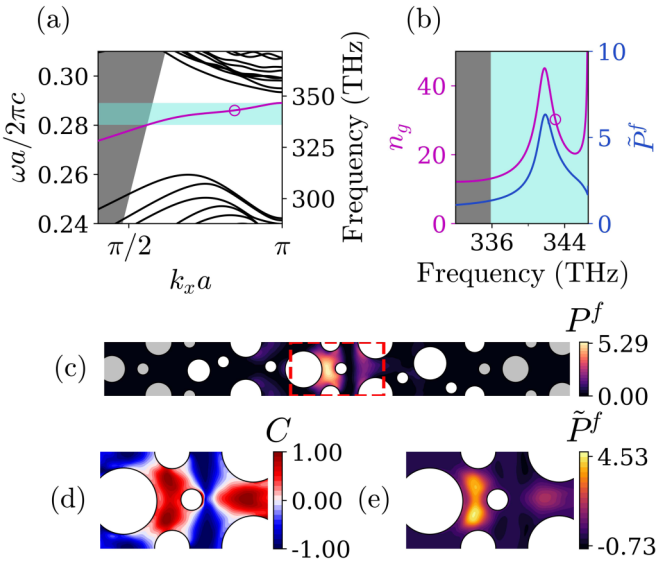

FIG. 3. Summary of design A. (a) Band structure. (b) Group index and the maximum chiral forward Purcell factor for the NT mode. The following fields are calculated at the circles in (a) and (b), where $n_g = 30.2$. (c) Forward Purcell factor P^f for $\boldsymbol{\mu} = \boldsymbol{\sigma}_-$, (d) the associated chiral directionality C, and (e) the associated chiral forward Purcell factor $\tilde{P}^f$. The holes which were not allowed to be modified during the optimization are drawn in gray, while the holes which were are drawn in white.

C. Improved designs

The results of our first optimization routine, designed to operate at a moderate group index, i.e., optimizing Eq. (17) and then Eq. (19), are summarized in Fig. 3. The band structure is shown in Fig. 3(a). The NT mode has a SM slow-light region with group index $n_g \approx 30$ deep inside the band gap and away from the Brillouin-zone edge. At a frequency where $n_g = 30$, indicated by circles in Figs. 3(a) and 3(b), the NT mode has $\max(\tilde{P}^f) = 4.5$, with $C = 0.91$. In the region at least 35 nm from the nearest hole edge where $C \geqslant 0.95$, the maximum forward Purcell factor is $\max(P^f) = 4.7$. This design satisfies our primary objective: the maximum Purcell factor in a region of high directionality far from a hole edge has been improved by an order of magnitude to values around our desired value of 5 [60–62].

Next, we optimize a waveguide to operate in the slow-light regime, well away from the band edge, optimizing Eq. (17) and then Eq. (20). The results are summarized in Fig. 4. For this design, we observe a slow-light, SM bandwidth with a maximum $n_g > 350$, deep inside the band gap and away from the mode edge [Figs. 4(a) and 4(b)]. For the mode with $n_g = 360$, we find $\max(\tilde{P}^f) = 48$, with $C = 0.98$. The position of $\max(\tilde{P}^f)$ is 40 nm away from the nearest hole edge. This is a two-orders-of-magnitude increase to the maximum chiral forward Purcell factor from the initial design. In the region at least 35 nm from the nearest hole

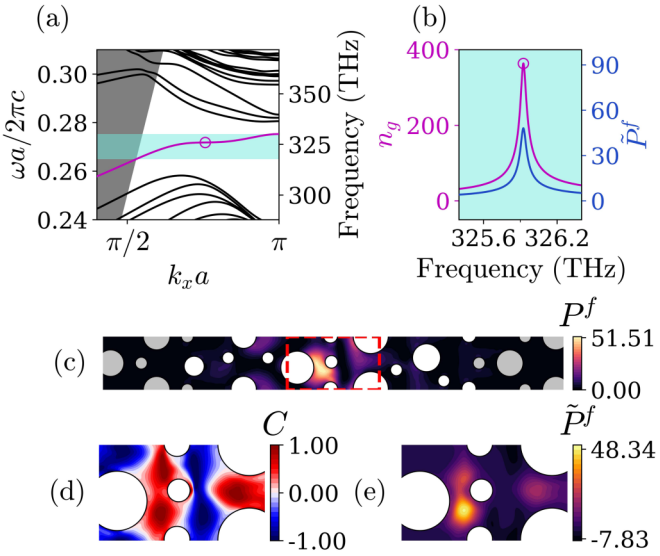

FIG. 4. Summary of design B. (a) Band structure. (b) Group index and the maximum chiral forward Purcell factor for the NT mode. The following fields are calculated at the circles in (a) and (b), where $n_g = 360$. (c) Forward Purcell factor P^f for $\boldsymbol{\mu} = \boldsymbol{\sigma}_-$, (d) the associated chiral directionality C, and (e) the associated chiral forward Purcell factor $\tilde{P}^f$. The holes which were not allowed to be modified during the optimization are drawn in gray, while the holes which were are drawn in white.

edge where $C \geqslant 0.95$, the maximum forward Purcell factor is $\max(P^f) = 50$.

In both of the improved designs, the glide-plane symmetry of a reflection about the x axis and translation in the x direction of $a/2$ has been broken. This has served to increase the overlap of the region of circular polarization with areas of high optical energy in the unit cell, therefore increasing the chiral forward Purcell factor. In Ref. [34], it was also found that topological PCWs can outperform those which have been specifically designed for chiral coupling, namely, the glide-plane waveguide.

IV. CONCLUSIONS

Using an efficient nanophotonic inverse-design approach, we have optimized state-of-the-art topological PCWs for directional QD-photon interactions. We presented PCWs designed to operate in the single-mode regime well away from the mode edge and with moderate (30) and large (360) group indices. The designs have maximum forward Purcell factors at least 35 nm away from the nearest hole edge with $C \geqslant 0.95$ of 4.7 and 50 at group indexes of 30 and 360, respectively.

Our optimized designs, while respecting all fabrication requirements, break the symmetry of the initial [21] and other previously reported [30,31,34,55,56] topological PCWs, as the first three original crystal unit cells on each side of the interface differ (see Appendix B for details). As a result, the T mode disappears, ensuring the SM operation of the remaining NT mode. Moreover, this broken symmetry leads to asymmetric (with respect to the direction of propagation, $\hat{x}$) field (and hence P^f) distributions. This is most noticeable for slow-light modes [see Fig. 4(c)] but can also be observed in the faster mode [see Fig. 3(c)]. In essence, our optimization further increases the chiral-projected local density of states by *borrowing* from other regions in a way that is not possible with standard, topological PCW designs. Our results demonstrate the power of efficient inverse optimization methods, providing a key to unlock the full potential of topological quantum photonics.

ACKNOWLEDGMENTS

We thank N. Martin, M. J. Mehrabad, A. Foster, and L. Wilson for useful discussions. This work was supported by the Natural Sciences and Engineering Research Council of Canada, the Canadian Foundation for Innovation, and Queen's University, Canada.

APPENDIX A: ADDITIONAL EDGE STATES EXISTING AT THE EDGES OF THE GME SUPERCELL

The GME method assumes two-dimensional periodicity. As the crystals on each side of the waveguide are inversion-symmetry partners, at the y limits of the GME waveguide unit cell a second topological waveguide is modeled. This is a legitimate design, although not the design of interest. As an example the band structure for the unit cell shown in Fig. 5(b) is plotted in Fig. 5(a). The unit cell contains two interfaces between the topologically distinct crystals, the first being the waveguide [21] which the optimization started from and the second being another topological waveguide which was previously described in Ref. [31].

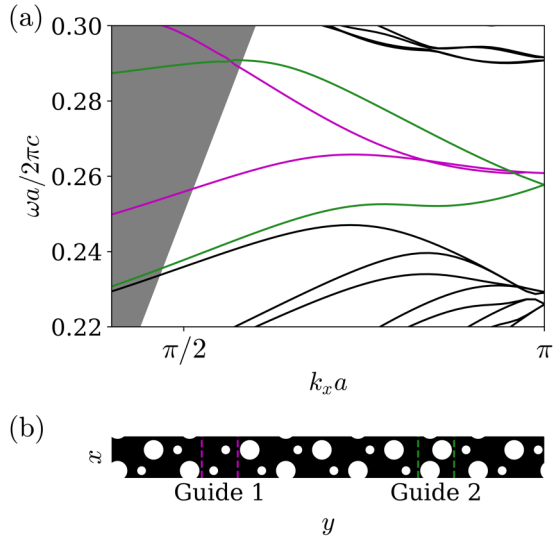

FIG. 5. (a) Band structure for the unit cell in (b). The modes existing at guide 1 are drawn in purple, the modes existing at guide 2 are drawn in green, and the bulk modes are drawn in black. (b) GME unit cell containing the waveguide which the optimization started from [21] and another waveguide [31].

TABLE I. Location and radius of the 12 holes, indexed by m, closest to the interface in the initial design. The x axis is at the center of the waveguide initial design; see Fig. 1 for the coordinate system.

m	$x[a]$	$y[a]$	$r[a]$
1	0.0000	−2.4537	0.2350
2	0.0000	−1.8764	0.1053
3	0.5000	−1.5877	0.2350
4	0.5000	−1.0104	0.1053
5	0.0000	−0.7217	0.2350
6	0.0000	−0.1443	0.1053
7	0.5000	0.1443	0.1053
8	0.5000	0.7217	0.2350
9	0.0000	1.0104	0.1053
10	0.0000	1.5877	0.2350
11	0.5000	1.8764	0.1053
12	0.5000	2.4537	0.2350

APPENDIX B: SPECIFICATIONS OF IMPROVED DESIGNS

In this Appendix, the positions and radii of holes in the initial and improved designs are provided. Table I lists the position and radii of the 12 holes closest to the interface in the initial design, which are the holes whose positions and radii were allowed to be modified during the optimizations. Table II lists the change in positions and radii of these holes for designs A and B.

TABLE II. Change in the location and radius of the 12 holes closest to the interface in designs A and B. The hole indexes m are the same as in Table I.

	m	$\Delta x[a]$	$\Delta y[a]$	$\Delta r[a]$
Design A	1	0.0316	−0.1168	−0.0349
	2	−0.1319	−0.2374	−0.0020
	3	−0.0121	−0.1065	0.0461
	4	0.4557	−0.2218	−0.0020
	5	0.0089	0.0994	0.0922
	6	−0.0059	0.2224	−0.0020
	7	−0.0078	−0.2666	0.0699
	8	−0.0134	−0.0060	0.0760
	9	0.1667	0.2083	−0.0020
	10	−0.1048	0.1439	0.0598
	11	−0.1484	0.2485	−0.0020
	12	0.0047	0.1063	−0.0591
Design B	1	0.0579	−0.1602	−0.0616
	2	−0.1001	−0.0970	−0.0020
	3	−0.0150	−0.0948	−0.0133
	4	0.4028	−0.2156	−0.0020
	5	0.0849	0.0470	0.0606
	6	−0.0244	0.1112	0.0068
	7	−0.0146	−0.1952	0.0227
	8	−0.0101	−0.0157	0.0801
	9	0.1269	0.1780	−0.0020
	10	−0.1016	0.1668	0.0126
	11	−0.1662	0.2031	−0.0020
	12	−0.0236	0.0983	−0.1173

[1] P. Lodahl, S. Mahmoodian, S. Stobbe, A. Rauschenbeutel, P. Schneeweiss, J. Volz, H. Pichler, and P. Zoller, Chiral quantum optics, Nature (London) **541**, 473 (2017).

[2] I. Söllner, S. Mahmoodian, S. L. Hansen, L. Midolo, A. Javadi, G. Kiršanskė, T. Pregnolato, H. El-Ella, E. H. Lee, J. D. Song, S. Stobbe, and P. Lodahl, Deterministic photon–emitter coupling in chiral photonic circuits, Nat. Nanotechnol. **10**, 775 (2015).

[3] K. Xia, G. Lu, G. Lin, Y. Cheng, Y. Niu, S. Gong, and J. Twamley, Reversible nonmagnetic single-photon isolation using unbalanced quantum coupling, Phys. Rev. A **90**, 043802 (2014).

[4] C. Sayrin, C. Junge, R. Mitsch, B. Albrecht, D. O'Shea, P. Schneeweiss, J. Volz, and A. Rauschenbeutel, Nanophotonic Optical Isolator Controlled by the Internal State of Cold Atoms, Phys. Rev. X **5**, 041036 (2015).

[5] M. Scheucher, A. Hilico, E. Will, J. Volz, and A. Rauschenbeutel, Quantum optical circulator controlled by a single chirally coupled atom, Science **354**, 1577 (2016).

[6] S. Pucher, C. Liedl, S. Jin, A. Rauschenbeutel, and P. Schneeweiss, Atomic spin-controlled non-reciprocal Raman amplification of fibre-guided light, Nat. Photonics **16**, 380 (2022).

[7] I. Shomroni, S. Rosenblum, Y. Lovsky, O. Bechler, G. Guendelman, and B. Dayan, All-optical routing of single photons by a one-atom switch controlled by a single photon, Science **345**, 903 (2014).

[8] F. T. Østfeldt, E. M. González-Ruiz, N. Hauff, Y. Wang, A. D. Wieck, A. Ludwig, R. Schott, L. Midolo, A. S. Sørensen, R. Uppu, and P. Lodahl, On-demand source of dual-rail photon pairs based on chiral interaction in a nanophotonic waveguide, PRX Quantum **3**, 020363 (2022).

[9] S. Mahmoodian, P. Lodahl, and A. S. Sørensen, Quantum Networks with Chiral-Light–Matter Interaction in Waveguides, Phys. Rev. Lett. **117**, 240501 (2016).

[10] V. S. C. Manga Rao and S. Hughes, Single quantum-dot Purcell factor and β factor in a photonic crystal waveguide, Phys. Rev. B **75**, 205437 (2007).

[11] A. Laucht, S. Pütz, T. Günthner, N. Hauke, R. Saive, S. Frédérick, M. Bichler, M.-C. Amann, A. W. Holleitner, M. Kaniber, and J. J. Finley, A Waveguide-Coupled On-Chip Single-Photon Source, Phys. Rev. X **2**, 011014 (2012).

[12] P. Lodahl, S. Mahmoodian, and S. Stobbe, Interfacing single photons and single quantum dots with photonic nanostructures, Rev. Mod. Phys. **87**, 347 (2015).

[13] K. Kuruma, H. Yoshimi, Y. Ota, R. Katsumi, M. Kakuda, Y. Arakawa, and S. Iwamoto, Topologically-protected single-photon sources with topological slow light photonic crystal waveguides, Laser Photonics Rev. **16**, 2200077 (2022).

[14] M. Arcari, I. Söllner, A. Javadi, S. Lindskov Hansen, S. Mahmoodian, J. Liu, H. Thyrrestrup, E. H. Lee, J. D. Song, S. Stobbe, and P. Lodahl, Near-Unity Coupling Efficiency of a Quantum Emitter to a Photonic Crystal Waveguide, Phys. Rev. Lett. **113**, 093603 (2014).

[15] P. C. Holz, S. Auchter, G. Stocker, M. Valentini, K. Lakhmanskiy, C. Rössler, P. Stampfer, S. Sgouridis, E. Aschauer, Y. Colombe, and R. Blatt, 2d linear trap array for quantum information processing, Adv. Quantum Technol. **3**, 2000031 (2020).

[16] R. Uppu, F. T. Pedersen, Y. Wang, C. T. Olesen, C. Papon, X. Zhou, L. Midolo, S. Scholz, A. D. Wieck, A. Ludwig, and P. Lodahl, Scalable integrated single-photon source, Sci. Adv. **6**, eabc8268 (2020).

[17] H. Le Jeannic, T. Ramos, S. F. Simonsen, T. Pregnolato, Z. Liu, R. Schott, A. D. Wieck, A. Ludwig, N. Rotenberg, J. J. García-Ripoll, and P. Lodahl, Experimental Reconstruction of the Few-Photon Nonlinear Scattering Matrix from a Single Quantum Dot in a Nanophotonic Waveguide, Phys. Rev. Lett. **126**, 023603 (2021).

[18] B. Lang, D. M. Beggs, A. B. Young, J. G. Rarity, and R. Oulton, Stability of polarization singularities in disordered photonic crystal waveguides, Phys. Rev. A **92**, 063819 (2015).

[19] B. Lang, D. P. S. McCutcheon, E. Harbord, A. B. Young, and R. Oulton, Perfect Chirality with Imperfect Polarization, Phys. Rev. Lett. **128**, 073602 (2022).

[20] A. B. Young, A. C. T. Thijssen, D. M. Beggs, P. Androvitsaneas, L. Kuipers, J. G. Rarity, S. Hughes, and R. Oulton, Polarization Engineering in Photonic Crystal Waveguides for Spin-Photon Entanglers, Phys. Rev. Lett. **115**, 153901 (2015).

[21] M. J. Mehrabad, A. P. Foster, R. Dost, E. Clarke, P. K. Patil, A. M. Fox, M. S. Skolnick, and L. R. Wilson, Chiral topological photonics with an embedded quantum emitter, Optica **7**, 1690 (2020).

[22] R. Su, S. Ghosh, T. C. H. Liew, and Q. Xiong, Optical switching of topological phase in a perovskite polariton lattice, Sci. Adv. **7**, eabf8049 (2021).

[23] L. O'Faolain, T. P. White, D. O'Brien, X. Yuan, M. D. Settle, and T. F. Krauss, Dependence of extrinsic loss on group velocity in photonic crystal waveguides, Opt. Express **15**, 13129 (2007).

[24] S. Hughes, L. Ramunno, J. F. Young, and J. E. Sipe, Extrinsic Optical Scattering Loss in Photonic Crystal Waveguides: Role of Fabrication Disorder and Photon Group Velocity, Phys. Rev. Lett. **94**, 033903 (2005).

[25] M. Patterson, S. Hughes, S. Combrié, N.-V.-Q. Tran, A. De Rossi, R. Gabet, and Y. Jaouën, Disorder-Induced Coherent Scattering in Slow-Light Photonic Crystal Waveguides, Phys. Rev. Lett. **102**, 253903 (2009).

[26] M. Patterson, S. Hughes, S. Schulz, D. M. Beggs, T. P. White, L. O'Faolain, and T. F. Krauss, Disorder-induced incoherent scattering losses in photonic crystal waveguides: Bloch mode reshaping, multiple scattering, and breakdown of the Beer-Lambert law, Phys. Rev. B **80**, 195305 (2009).

[27] L. C. Andreani and D. Gerace, Light–matter interaction in photonic crystal slabs, Phys. Status Solidi B **244**, 3528 (2007).

[28] E. Kuramochi, M. Notomi, S. Hughes, A. Shinya, T. Watanabe, and L. Ramunno, Disorder-induced scattering loss of line-defect waveguides in photonic crystal slabs, Phys. Rev. B **72**, 161318(R) (2005).

[29] A. Petrov, M. Krause, and M. Eich, Backscattering and disorder limits in slow light photonic crystal waveguides, Opt. Express **17**, 8676 (2009).

[30] M. I. Shalaev, W. Walasik, A. Tsukernik, Y. Xu, and N. M. Litchinitser, Robust topologically protected transport in photonic crystals at telecommunication wavelengths, Nat. Nanotechnol. **14**, 31 (2019).

[31] X.-T. He, E.-T. Liang, J.-J. Yuan, H.-Y. Qiu, X.-D. Chen, F.-L. Zhao, and J.-W. Dong, A silicon-on-insulator slab for topological valley transport, Nat. Commun. **10**, 872 (2019).

[32] S. Arora, T. Bauer, R. Barczyk, E. Verhagen, and L. Kuipers, Direct quantification of topological protection in symmetry-protected photonic edge states at telecom wavelengths, Light Sci. Appl. **10**, 9 (2021).

[33] C. A. Rosiek, G. Arregui, A. Vladimirova, M. Albrechtsen, B. V. Lahijani, R. E. Christiansen, and S. Stobbe, Observation of strong backscattering in valley-Hall photonic topological interface modes, arXiv:2206.11741.

[34] N. V. Hauff, H. Le Jeannic, P. Lodahl, S. Hughes, and N. Rotenberg, Chiral quantum optics in broken-symmetry and topological photonic crystal waveguides, Phys. Rev. Res. **4**, 023082 (2022).

[35] Y. Zhao, Y. Zhang, Q. Wang, and H. Hu, Review on the optimization methods of slow light in photonic crystal waveguide, IEEE Trans. Nanotechnol. **14**, 407 (2015).

[36] J. Li, T. P. White, L. O'Faolain, A. Gomez-Iglesias, and T. F. Krauss, Systematic design of flat band slow light in photonic crystal waveguides, Opt. Express **16**, 6227 (2008).

[37] J. Li, L. O'Faolain, S. A. Schulz, and T. F. Krauss, Low loss propagation in slow light photonic crystal waveguides at group indices up to 60, Photonics Nanostruct. Fundam. Appl. **10**, 589 (2012).

[38] D. Mori and T. Baba, Wideband and low dispersion slow light by chirped photonic crystal coupled waveguide, Opt. Express **13**, 9398 (2005).

[39] B. Rigal, K. Joanesarson, A. Lyasota, C. Jarlov, B. Dwir, A. Rudra, I. Kulkova, and E. Kapon, Propagation losses in photonic crystal waveguides: Effects of band tail absorption and waveguide dispersion, Opt. Express **25**, 28908 (2017).

[40] S. Mahmoodian, K. Prindal-Nielsen, I. Söllner, S. Stobbe, and P. Lodahl, Engineering chiral light-matter interaction in photonic crystal waveguides with slow light, Opt. Mater. Express **7**, 43 (2017).

[41] S. Molesky, Z. Lin, A. Y. Piggott, W. Jin, J. Vucković, and A. W. Rodriguez, Inverse design in nanophotonics, Nat. Photonics **12**, 659 (2018).

[42] M. Minkov, I. A. D. Williamson, L. C. Andreani, D. Gerace, B. Lou, A. Y. Song, T. W. Hughes, and S. Fan, Inverse design of photonic crystals through automatic differentiation, ACS Photonics **7**, 1729 (2020).

[43] A. Y. Piggott, J. Lu, K. G. Lagoudakis, J. Petykiewicz, T. M. Babinec, and J. Vučković, Inverse design and demonstration of a compact and broadband on-chip wavelength demultiplexer, Nat. Photonics **9**, 374 (2015).

[44] R. E. Christiansen, F. Wang, and O. Sigmund, Topological Insulators by Topology Optimization, Phys. Rev. Lett. **122**, 234502 (2019).

[45] N. Mann, S. Combrié, P. Colman, M. Patterson, A. D. Rossi, and S. Hughes, Reducing disorder-induced losses for slow light photonic crystal waveguides through Bloch mode engineering, Opt. Lett. **38**, 4244 (2013).

[46] L. C. Andreani and D. Gerace, Photonic-crystal slabs with a triangular lattice of triangular holes investigated using a

guided-mode expansion method, Phys. Rev. B **73**, 235114 (2006).

[47] E. Sauer, Theory and computation of intrinsic propagation losses and disorder-induced modes in topological photonic crystal waveguides using mode expansion techniques, Ph.D. thesis, Queen's University, Canada, 2021.

[48] J. P. Vasco and S. Hughes, Statistics of Anderson-localized modes in disordered photonic crystal slab waveguides, Phys. Rev. B **95**, 224202 (2017).

[49] E. Sauer, J. P. Vasco, and S. Hughes, Theory of intrinsic propagation losses in topological edge states of planar photonic crystals, Phys. Rev. Res. **2**, 043109 (2020).

[50] M. Minkov, I. Williamson, and S. Fan, LEGUME: Differentiable guided mode expansion methods, GitHub, https://github.com/fancompute/legume.

[51] S. Franke, J. Ren, M. Richter, A. Knorr, and S. Hughes, Fermi's Golden Rule for Spontaneous Emission in Absorptive and Amplifying Media, Phys. Rev. Lett. **127**, 013602 (2021).

[52] D. Maclaurin, D. Duvenaud, M. Johnson, and J. Townsend, AUTOGRAD, GitHub, https://github.com/HIPS/autograd.

[53] A. Michaels and E. Yablonovitch, Leveraging continuous material averaging for inverse electromagnetic design, Opt. Express **26**, 31717 (2018).

[54] H. Yoshimi, T. Yamaguchi, Y. Ota, Y. Arakawa, and S. Iwamoto, Slow light waveguides in topological valley photonic crystals, Opt. Lett. **45**, 2648 (2020).

[55] H. Yoshimi, T. Yamaguchi, R. Katsumi, Y. Ota, Y. Arakawa, and S. Iwamoto, Experimental demonstration of topological slow light waveguides in valley photonic crystals, Opt. Express **29**, 13441 (2021).

[56] S. Barik, A. Karasahin, C. Flower, T. Cai, H. Miyake, W. DeGottardi, M. Hafezi, and E. Waks, A topological quantum optics interface, Science **359**, 666 (2018).

[57] L. Lu, J. D. Joannopoulos, and M. Soljačić, Topological photonics, Nat. Photonics **8**, 821 (2014).

[58] M. B. de Paz, C. Devescovi, G. Giedke, J. J. Saenz, M. G. Vergniory, B. Bradlyn, D. Bercioux, and A. García-Etxarri, Tutorial: Computing topological invariants in 2D photonic crystals, Adv. Quantum Technol. **3**, 1900117 (2020).

[59] T. Pregnolato, X.-L. Chu, T. Schröder, R. Schott, A. D. Wieck, A. Ludwig, P. Lodahl, and N. Rotenberg, Deterministic positioning of nanophotonic waveguides around single self-assembled quantum dots, APL Photonics **5**, 086101 (2020).

[60] C. Gustin and S. Hughes, Pulsed excitation dynamics in quantum-dot–cavity systems: Limits to optimizing the fidelity of on-demand single-photon sources, Phys. Rev. B **98**, 045309 (2018).

[61] N. Somaschi, V. Giesz, L. D. Santis, J. C. Loredo, M. P. Almeida, G. Hornecker, S. L. Portalupi, T. Grange, C. Antón, J. Demory, C. Gómez, I. Sagnes, N. D. Lanzillotti-Kimura, A. Lemaítre, A. Auffeves, A. G. White, L. Lanco, and P. Senellart, Near-optimal single-photon sources in the solid state, Nat. Photonics **10**, 340 (2016).

[62] X. Ding, Y. He, Z.-C. Duan, N. Gregersen, M.-C. Chen, S. Unsleber, S. Maier, C. Schneider, M. Kamp, S. Höfling, C.-Y. Lu, and J.-W. Pan, On-Demand Single Photons with High Extraction Efficiency and Near-Unity Indistinguishability from a Resonantly Driven Quantum Dot in a Micropillar, Phys. Rev. Lett. **116**, 020401 (2016).

[63] D. P. Kingma and J. Ba, Adam: A method for stochastic optimization, arXiv:1412.6980.